Materials Science & Engineering A 618 (2014) 323–334

Contents lists available at ScienceDirect

Materials Science & Engineering A

journal homepage: www.elsevier.com/locate/msea

Resistance spot welding of AZ series magnesium alloys: Effects of aluminum content on microstructure and mechanical properties

Seyedtirdad Niknejad [a,*], Lei Liu [b], Mok-Young Lee [c], Shahrzad Esmaeili [a], Norman Y. Zhou [a]

[a] Department of Mechanical and Mechatronics Engineering, University of Waterloo, 200 University Ave., Waterloo, Ontario, Canada N2l 3G1
[b] Department of Mechanical Engineering, Tsinghua University, Beijing 100084, China
[c] Research Institute of Industrial Science & Technology, Pohang 790-600, South Korea

ARTICLE INFO

Article history:
Received 6 May 2014
Received in revised form
5 August 2014
Accepted 5 August 2014
Available online 14 August 2014

Keywords:
Resistance spot welding
AZ magnesium alloys
Weld strength
Failure modes
Post-weld heat treatment
β-$Mg_{17}(Al,Zn)_{12}$ phase

ABSTRACT

The microstructural evolution of the spot welded AZ31, AZ61 and AZ80 magnesium alloys was studied via optical and scanning electron microscopy. As the Al content of the magnesium base alloy increased from 3 wt% (AZ31) to 6% (AZ61) and 8% (AZ80), columnar to equi-axed dendrite transition and grain refinement in the fusion zone were enhanced. However, the increasing amount of the β-$Mg_{17}(Al,Zn)_{12}$ phase in the heat affected zone (HAZ) and fusion zone (FZ) resulted in the reduction of the tensile shear strengths of the AZ61 and AZ80 welds compared to those of AZ31 welds. Moreover, in the tensile-shear testing, the AZ61 and AZ80 welds failed in the heat affected zone along the fusion boundary, because micro-cracking occurred preferentially at the interfaces between β particles and Mg matrix. Post-weld solutionizing treatment was found to significantly reduce the quantity of β particles in heat affected and fusion zones of AZ61 and AZ80 welds. This led to an increase in the weld strengths of AZ61 and AZ80 alloys because the heat treatment eliminated the β particles and cracks propagated into the coarse-grained heat affected zone and then base material. For the heat treated welds, grain size was found as a major factor in the failure mode.

1. Introduction

Resistance spot welding (RSW) has been widely used in joining of sheet metals for auto body assembly. RSW has also been an interesting subject for research, due to the unique geometry and location of the fusion zone (FZ) relative to the base materials [1–4]. A natural crack/notch is produced along the spot nugget circumference, which intensifies the stresses during static or cyclic loading. Thus, the load capacity of a spot welded structure depends strongly on the fracture properties of the material within this region i.e. fusion zone, heat affected zone and base material. The alloys based on the Mg–Al–Zn ternary system known as AZ are the most widely used magnesium alloys in the automotive industry owing to their excellent castability and recyclability, low cost and relatively high strength. The thermal cycle of fusion welding processes results in liquation and formation of β-$Mg_{17}Al_{12}$ intermetallics (space group $I\bar{4}3m$ and $a \sim 10.6$ Å [5]) in heat affected zone (HAZ) [6–9]. Generally, fracture properties of metallic materials are deteriorated by the presence of incoherent particles located within the grain matrix or along the grain boundaries (GBs). This is due to decohesion of particle/matrix at the interface, which facilitates the crack propagation [10,11]. Formation of the β intermetallics has been reported to be detrimental to the ductility and fracture toughness of the as cast AZ alloys [12–15]. It was reported that the dissolution of the intermetallics increased the strength and ductility of AZ91 Mg alloy by changing the fracture mechanism from inter-granular to trans-granular [16].

The fracture properties of magnesium alloys are severely affected by the grain morphology as well as grain size [17–19]. Heterogeneous nucleation rate is reported to be increased by the addition of secondary phase particles with high melting point, which promotes columnar to equi-axed dendrite transition and grain refinement. This results in improvement of RSW strength due to increased resistance to crack initiation and propagation [20–23].

In our previous work, the post-weld heat treatment was found to improve the weld strength in RSW of AZ80 alloy [24]. The main objective of the current work was to study the effects of Al content, as the major alloying element in the AZ alloys, on the microstructural features and mechanical properties of RSW. The capability of post-weld heat treatment to improve the mechanical strength of RSW of magnesium alloys with different Al contents has also been examined.

* Corresponding author. Tel.: +1 519 8884567x33326.
E-mail address: snikneja@uwaterloo.ca (S. Niknejad).

http://dx.doi.org/10.1016/j.msea.2014.08.013
0921-5093/

Table 1
Chemical composition of the three AZ alloys and tensile properties in rolling direction.

	Al(wt. %)	Zn(wt. %)	Mn(wt. %)	Tensile Strength (MPa)	Elongation (%)
AZ31	2.9	1.1	0.3	260	22.5
AZ61	6.1	1.2	0.5	284	14.3
AZ80	7.7	0.7	0.2	336	8.3

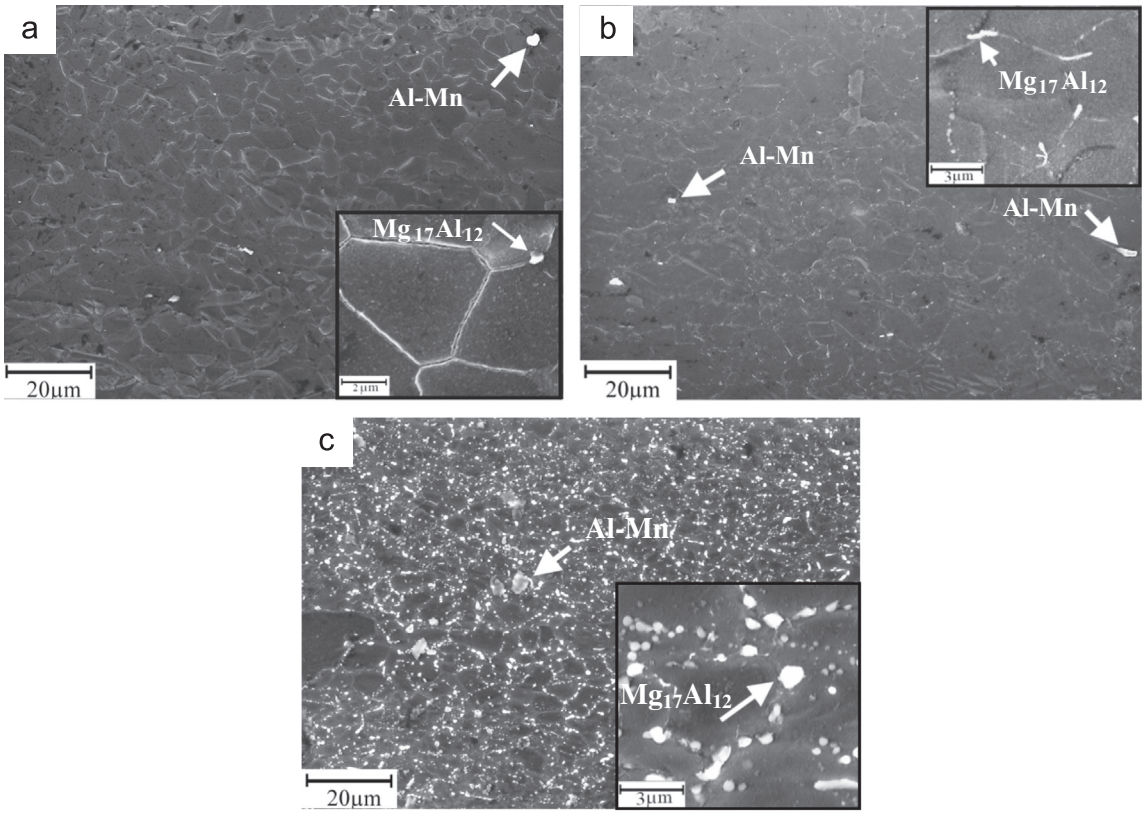

Fig. 1. SEM microstructure of three as-received AZ alloys (a) AZ31, (b) AZ61, (c) AZ80.

2. Experimental procedure

AZ31, AZ61 and AZ80 hot rolled sheets, 2 mm in thickness, were used for the current research. Table 1 lists the chemical composition and the tensile properties of the as-received alloys. The base metal (BM) microstructures are shown in Fig. 1. The bright particles mostly observed at the grain boundaries (GBs) were enriched in Mg and Al and found to be β-$Mg_{17}Al_{12}$ phase [25,26]. The microstructure in AZ31 comprised single phase α-Mg with very few traces of β particles in GBs. A uniform distribution of β was observed in the GBs of the microstructure in AZ61. Coarse β particles were present both in the grains and GBs of the AZ80 microstructure. The three alloys contained Al–Mn particles mostly observed inside the grains as shown in Fig. 1. Rectangular specimens of 100 mm × 25 mm were prepared for the RSW according to AWS-D17.2 standard (Fig. 2). RSW was performed using a medium frequency DC spot welding machine (Centerline Ltd., Windsor, ON, Canada). The same welding parameters were used for the RSW of all the weld samples in order to maintain a consistent spot nugget size for all weld samples (9.5–9.9 mm in diameter). The post-weld heat treatment (PWHT) was performed above the solvus temperature of the two alloys at 400 °C for 0.5 h followed by cooling in air. The PWHT temperature was selected based on the thermodynamic calculation by FactSage software for dissolution of the $Mg_{17}Al_{12}$ phase. The microstructures of the weld samples were examined by optical microscopy (OM) and scanning electron microscopy (SEM) after acetic-picral etching.

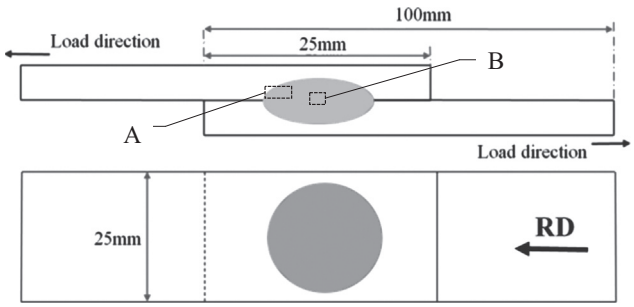

Fig. 2. Schematic diagram of RSW specimens.

For transmission electron microscopy (TEM), thin samples were cut-off from the weld cross section with a thickness of 400 μm. Mechanical thinning of discs was carried out to a thickness of 100 μm. The TEM foils were electro-polished in a Tenupol 5 (Struers, Ballerup, Denmark) double jet polishing unit in a solution of 5.3 g lithium chloride (LiCl), 11.16 g magnesium perchlorate ($Mg(ClO_4)_2$), 500 ml methanol, 100 ml butyl cellosolve at −45 °C. The foils were afterwards subjected to 2 h ion milling on a Gatan 691 precision ion polishing system (PIPS) in order to remove the

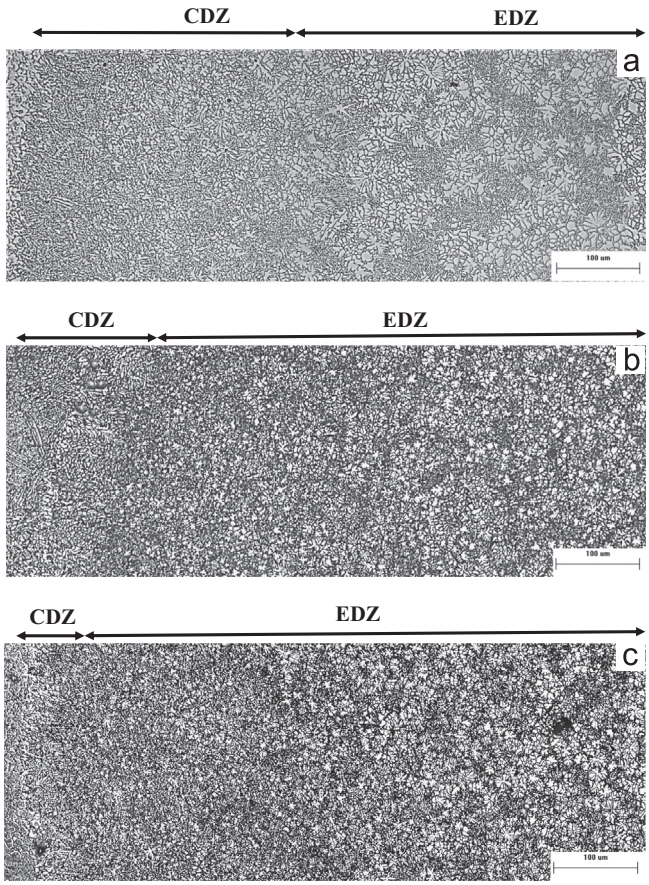

Fig. 3. Microstructure morphology across the RSW (view A as highlighted in Fig. 2) (a) AZ31; (b) AZ61 and (c) AZ80.

surface oxide layer. For the TEM analysis of the HAZ, sample preparation was done via focused ion beam (FIB). FIB milling was performed with a Zeiss NVision 40. The FIB lift-out method [27] was utilized. A thin layer of tungsten was deposited on the specimen to protect it during the milling process. The FIB was performed using Ga liquid metal ion source. A Ga beam operating at 30 KV excavated the specimen from both sides to a depth of 12 μm. The bottom of the lamella was cut out and the lamella was then lifted out and attached to a TEM grid. The lamella was further thinned to electron transparency using reduced voltage and current. Final thinning was performed at 1 kV to reduce the amorphous layer. High resolution transmission electron microscopy (HR-TEM) and energy dispersive spectroscopy (EDS) analysis was performed in a JEOL 2010F TEM (field emission gun with a point to point resolution of 0.23 nm) equipped with an EDAX system operating at a voltage of 200 kV.

Five tensile shear specimens were prepared for each condition to evaluate the mechanical properties (Fig. 2). To study the crack propagation path the tensile testing was stopped after the maximum load was reached, i.e. peak hold. The peak hold specimens were afterwards examined by the OM and SEM to investigate the location and causes of cracks.

3. Results

3.1. General microstructure across the weld and phase analysis

Fig. 3 shows the microstructure across the RSW for the three alloys. A columnar dendrite zone (CDZ) existed adjacent to the fusion boundary. By advancing towards the center of the weld nugget, the equi-axed dendrite zone (EDZ) was observed comprised of the flower-like dendrites. The average length of the columnar dendrite zone was measured to be 320 μm, 170 μm and

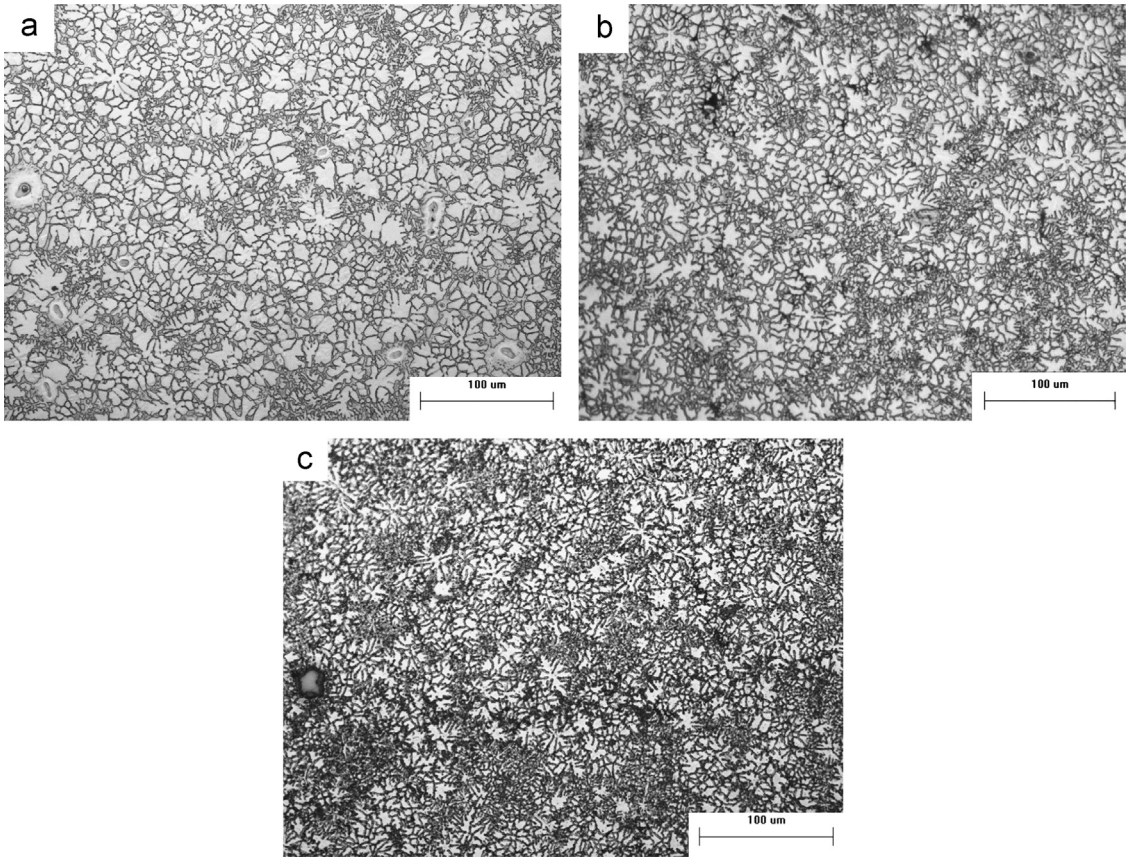

Fig. 4. Optical microstructure of the FZ in the center of nugget (view B as highlighted in Fig. 2) (a) AZ31; (b) AZ61 and (c) AZ80.

80 μm for AZ31, AZ61 and AZ80 RSW respectively. Fig. 4 shows typical optical microstructure of the fusion zone (FZ) in the center of the weld nuggets. The size of the dendrites decreased from AZ31 to AZ80. The diameter of the flowerlike dendritic structures was measured to be 31 μm, 20 μm and 16 μm for AZ31, AZ61 and AZ80 welds respectively.

Fig. 5 shows the SEM microstructures of the FZ and HAZ of the three welds. Worm-like (bright in color) particles enriched in Al (25–34 at%Al was detected by EDS) were found in the inter-dendritic regions of the FZ. Small traces of Zn (max 4 at%) were also detected in the particles. These particles were again found to be β phase [6,7], which were formed by the eutectic reaction due to non-equilibrium solidification. Zinc can be dissolved into the β phase forming a $Mg_{17}(Al,Zn)_{12}$ compound. The volume fraction of these particles increased from AZ31 to AZ80.

Worm-like β particles were found as continuous networks in the GBs of HAZ in high Al alloys, especially AZ80; however, only small amounts of β particles were found in GBs of HAZ in AZ31. It appeared that localized melting also occurred within the HAZ grains. This has been confirmed by observation of globular particles of the β phase inside the grains (Fig. 5b,d,f). Close observation revealed particle free zones (PFZ) essentially adjacent to the GB particles (Fig. 5b,d,f). During the solidification of the solute rich GB melt, first the α-Mg phase is formed depleted of the solute pushing the solute atoms to the remaining liquid. Thus, the β particles are unlikely to form in the PFZ. The mechanisms responsible for the formation of β phase in HAZ are different depending on the chemical composition and microstructure of the BM:

- For high Al content alloys (AZ61 and AZ80), the β particles pre-existed in the GBs, as they remained undissolved during the sheet metal production. At the HAZ due to rapid heating to the eutectic temperature (T_E), the β phase reacted with the surrounding α matrix and formed a liquid eutectic (C_E) layer at the GBs.
- For AZ31 alloy, the formation of β particles indicated that that liquation occurred in the GBs of the HAZ (Fig. 5b) even though very few traces of the β phase were detected in the microstructure of AZ31 alloy (Fig. 2b). This can be explained by a mechanism proposed by Huang et al., in which HAZ liquation of

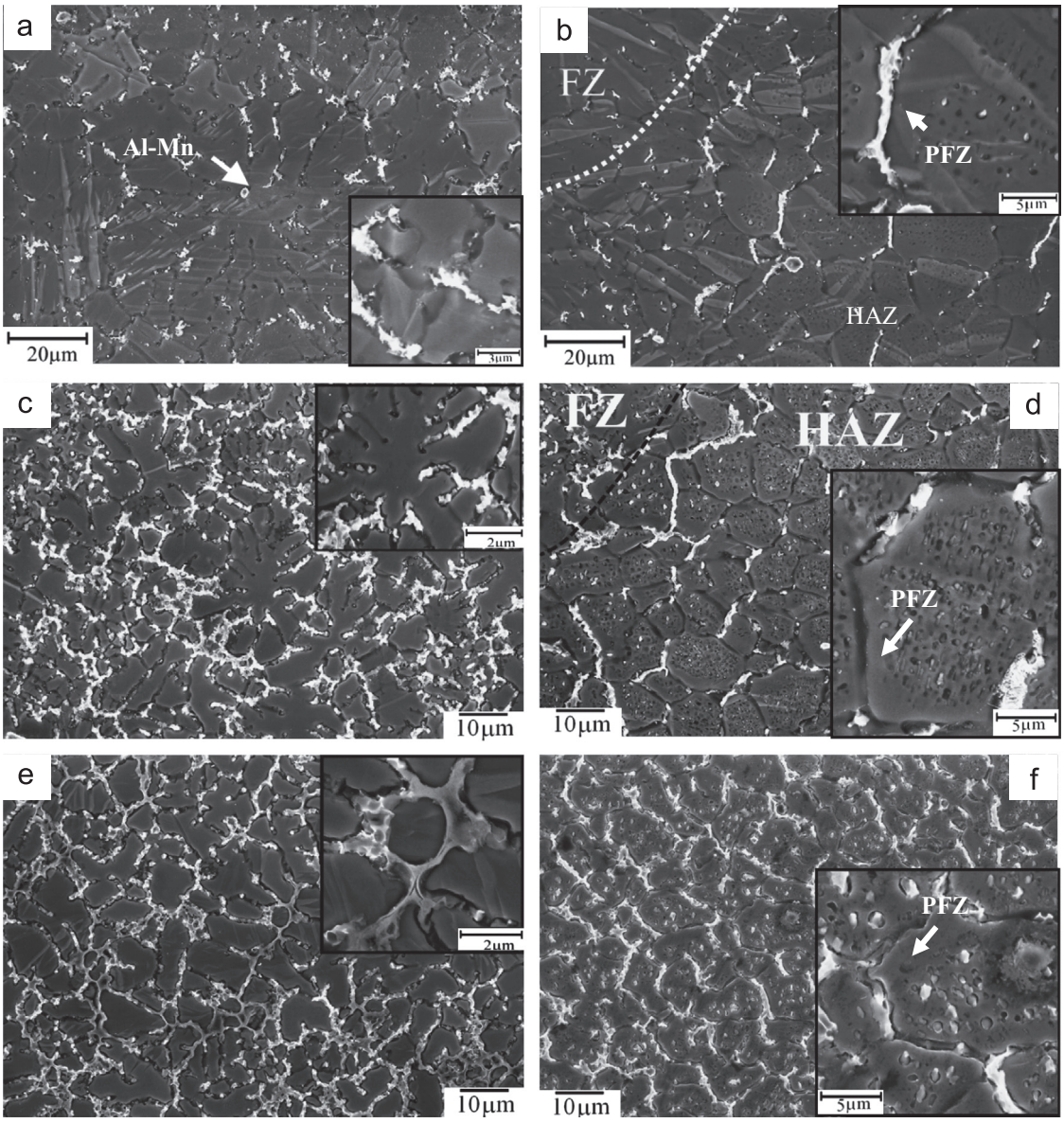

Fig. 5. SEM microstructure of the FZ and HAZ for AZ31 (a,b); AZ61 (c,d) and AZ80 (e,f).

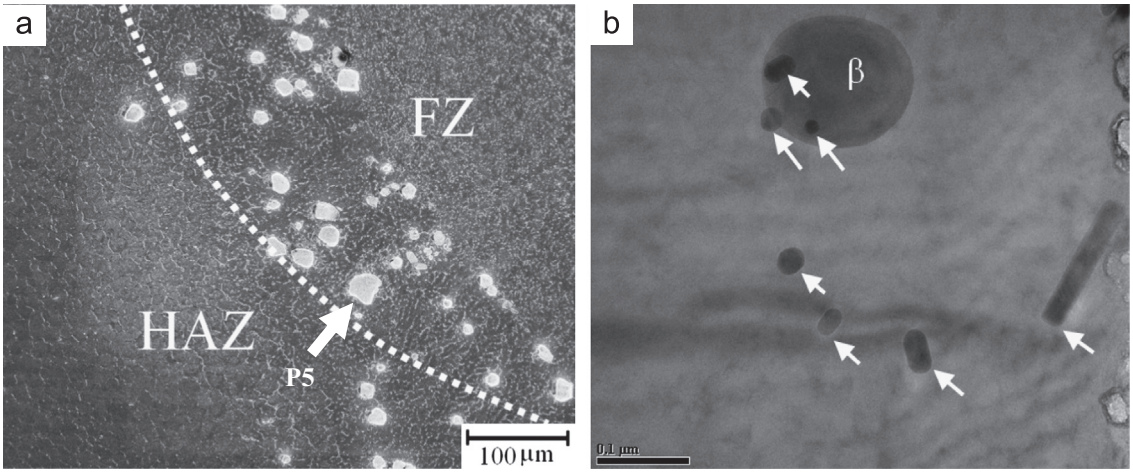

Fig. 6. (a) Microstructure near the fusion boundary of AZ80 and (b) TEM image of the sub-micron Al–Mn (highlighted by white arrows) and $Mg_{17}Al_{12}$ particles.

aluminum alloys occurs without the presence of secondary phase particles [28]. As the concentration of the solute atoms was relatively higher in GBs of BM, the liquation occurred preferentially in these regions.

Al–Mn rich particles were also detected inside the FZ as shown typically in Fig. 5a. However very large Al–Mn particles were concentrated along the fusion boundary of all the three welds. Fig. 6a shows a typical microstructure of AZ80 at the fusion boundary. The Al–Mn particles, existing in the BM microstructures, were significantly smaller than the ones observed in the fusion boundaries. The thermodynamic calculations by FactSage [29] predicted the formation of Al_8Mn_5 phase at a temperature above the liquidus temperature of α-Mg. Thus, these particles were likely to be formed as a result of chemical reaction during welding and were dragged away from the melt to the fusion boundary; however, the smaller particles remained suspended into the melt as observed typically in Fig. 5a. Nano-scale Al–Mn particles were also found by the TEM analysis of FZ (Fig. 6b). As observed, the nano-sized Al–Mn particles frequently have elongated morphologies. These particles can either be formed during the solidification of the weld or they are the un-melted particles from the BM, as the melting temperature of the Al_8Mn_5 was reported to be 1048–1191 °C [30]. This temperature range is higher than the peak temperature of the weld zone reported for RSW of magnesium alloys (around 770 °C [31]).

3.2. TEM study of Mg–Al intermetallics

Fig. 7 shows a GB β particle and the corresponding HR-TEM image at the interface. The bright particle was characterized by selected area electron diffraction (SAED) pattern, as β phase with BCC structure (a=10.61 Å). Based on Fig. 7b, the planar relationship for this interface can be defined as

$(0\,0\,0\,2)_\alpha // (0\,1\,1)_\beta$,

Fig. 8a demonstrates a typical intra-granular β in the HAZ. Fig. 8b,c shows the SAED patterns corresponding to the Mg and $Mg_{17}Al_{12}$ located along the $[5\,\bar{1}\,\bar{4}\,3]_\alpha$ and $[\bar{1}\,1\,1]_\beta$ respectively. It was observed in the SAED pattern corresponding to the $Mg/Mg_{17}Al_{12}$ interface (Fig. 8d,e) that the diffraction spot of $(3\,3\,0)$ of β is superimposed on that of $(0\,\bar{1}\,\bar{1}\,1)$ of Mg. The crystallographic planar relationship at the interface (zone 3 in Fig. 8a) was determined to be:

$(0\,\bar{1}\,\bar{1}\,\bar{1})_\alpha // (3\,3\,0)_\beta$.

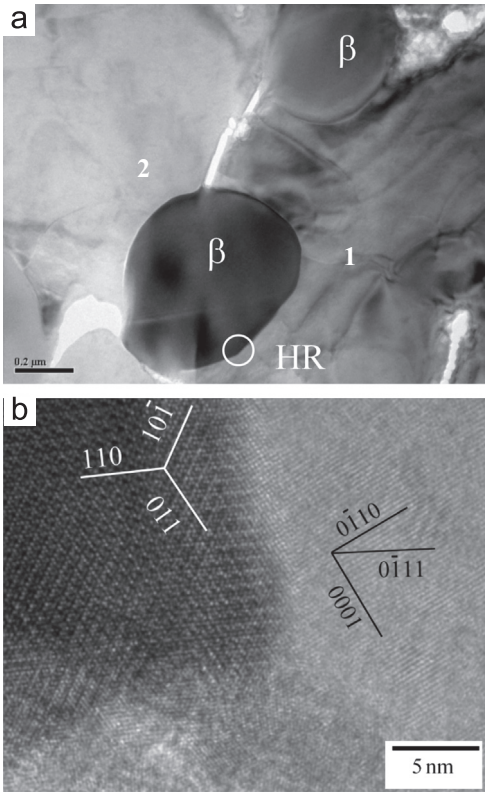

Fig. 7. TEM images of $Mg_{17}Al_{12}$ particle in the FZ of AZ80 (a) TEM image of intergranular particle; (b) HRTEM image for the area marked by a white circle in (a) along the $[2\,\bar{1}\,\bar{1}\,0]_\alpha/[1\,\bar{1}\,1]_\beta$ direction.

3.3. Effects of PWHT on weld microstructure

The particles at GBs were partially dissolved into the matrix of FZ and HAZ, during the PWHT, as observed in Fig. 9. The continuous networks of β phase at the GBs of the HAZ in AZ61 and AZ80 were disrupted and few isolated particles remained (see Figs. 9d,f).

Fig. 10 compares the grain size in the BM, as-welded HAZ and heat-treated HAZ microstructures. Significant increase in the grain size of HAZ was observed in all the welds in the as welded condition. Grain growth was more pronounced in the HAZ of AZ31 (× 2.7) than in the HAZ of AZ61 (× 1.5) and AZ80 (× 2). Such

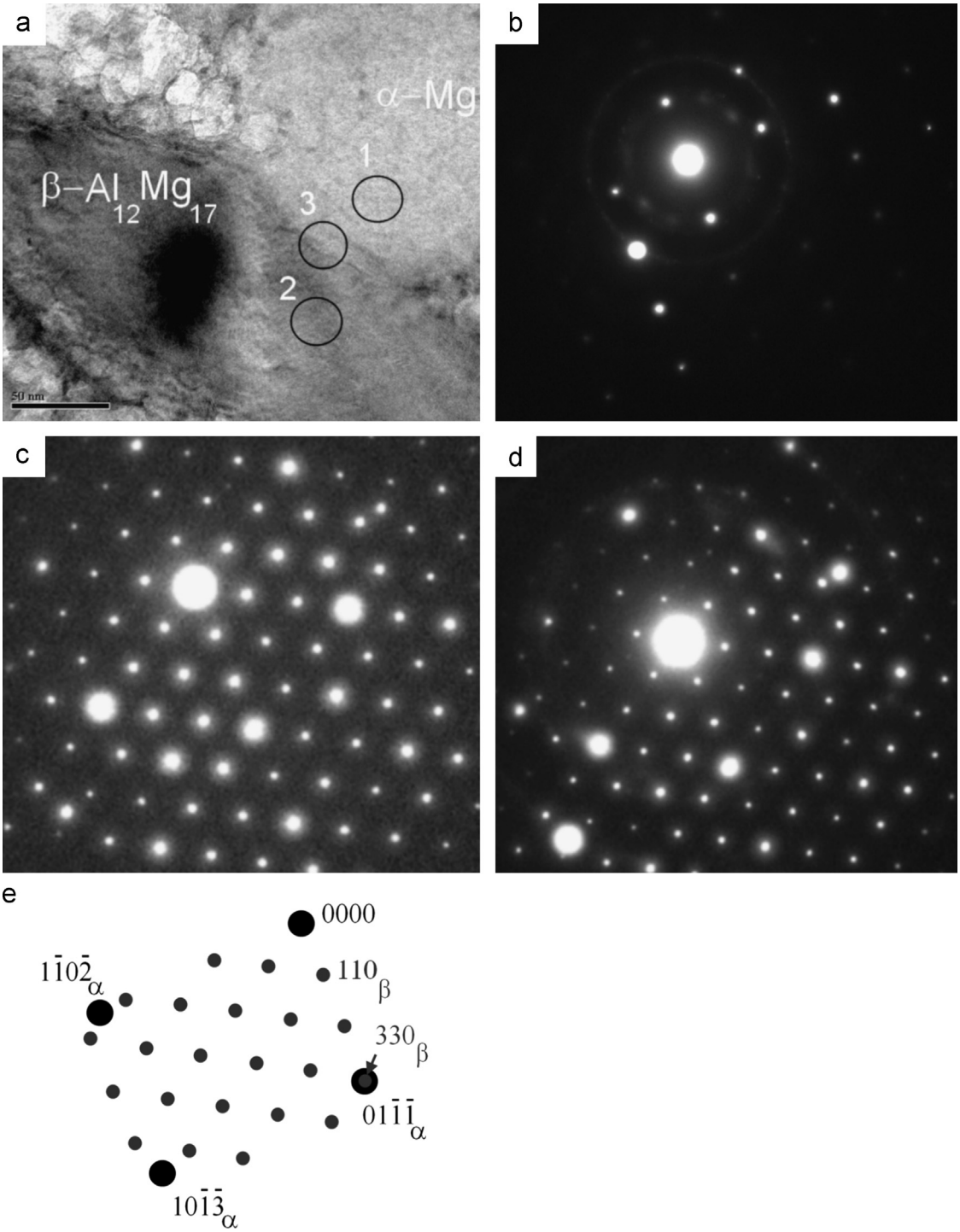

Fig. 8. (a) TEM image of $Mg_{17}Al_{12}$ particle in the HAZ of AZ80; (b) SAED of Mg matrix in area 1 (incident beam//[**5 $\bar{1}$ $\bar{4}$ 3**]); (c) SAED of $Mg_{17}Al_{12}$ particle in area 2 (incident beam//[**$\bar{1}$ 1 1**]); (c) SAED of Mg/$Mg_{17}Al_{12}$ interface in area 3 and (e) its schematic representation in $[\mathbf{5\ \bar{1}\ \bar{4}\ 3}]_\alpha/[\mathbf{\bar{1}\ 1\ 1}]_\beta$ direction.

an observation can be explained as follows: During the welding process, grain growth occurred in the HAZ, at temperatures, above the effective grain coarsening temperature (i.e. the single α phase region in the phase diagram); however, significant GB liquation retarded further grain growth. The solute-rich liquid film penetrated to the GBs and pinned them due to wetting action [32,33]. Since the liquid film had almost the same composition of the adjacent solid, the S–L interfacial energy was low [34] and the liquid film essentially wet the GBs [34]. No further grain growth occurred until the microstructure cooled down below the solidus of solute-rich liquid. Consequently, the thermal cycle of the HAZ in AZ61 and AZ80 led to incomplete grain growth because of significant liquation. Due to dissolution of the GBs in the HAZ of AZ61 and AZ80 during the PWHT, further grain growth occurred at large scale as indicated in Fig. 10. The unpinning of grain boundaries by the secondary phase particle dissolution has been reported to lead to explosive grain growth in the HAZ of nickel-based alloys [35]. Since insignificant liquation occurred in AZ31, the pinning of the grain boundaries by the wetting action was less than what occurred in the high Al content alloys. Thus, grain

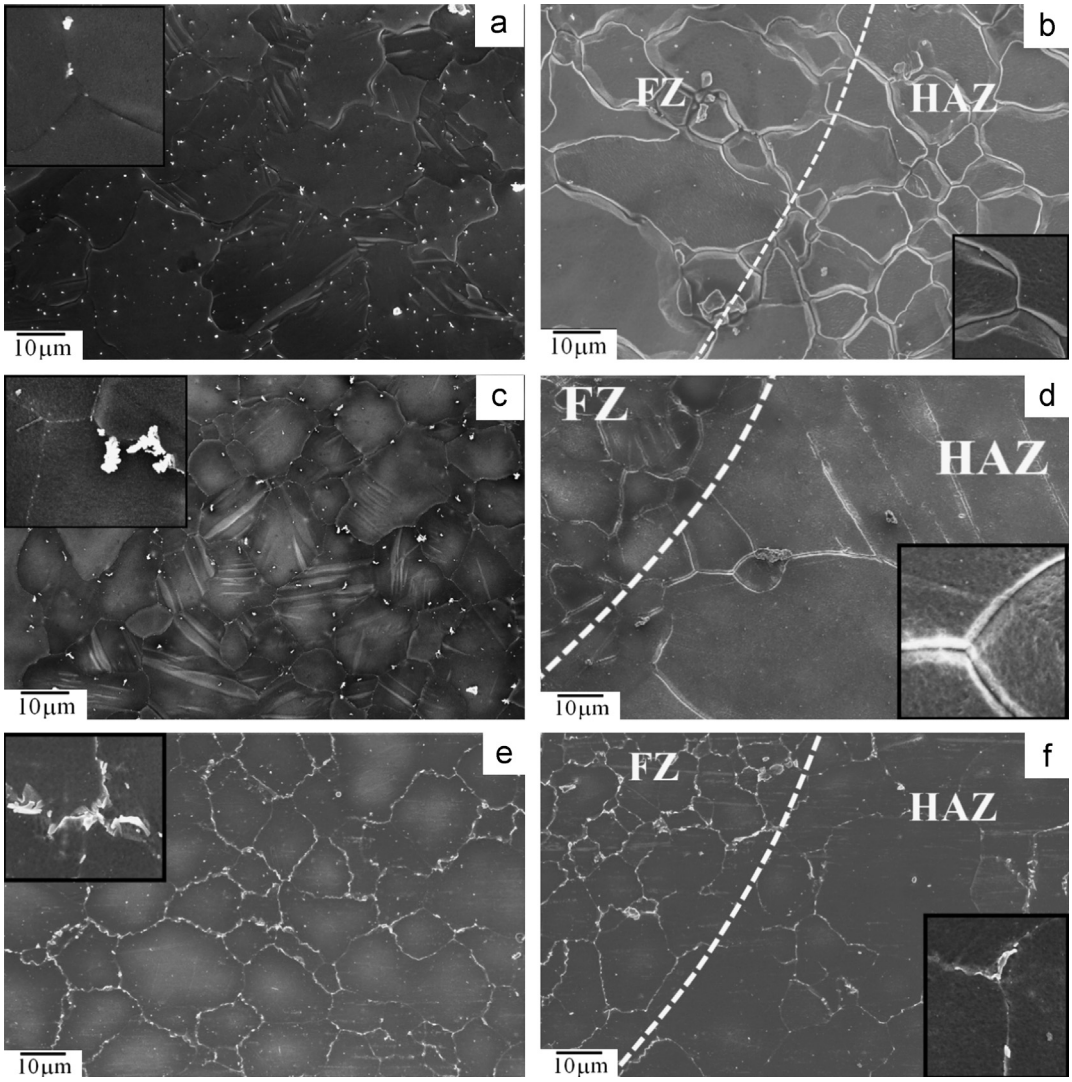

Fig. 9. SEM microstructure of the post-weld heat treated FZ and HAZ for AZ31 (a,b), AZ61 (c,d) and AZ80 (e,f).

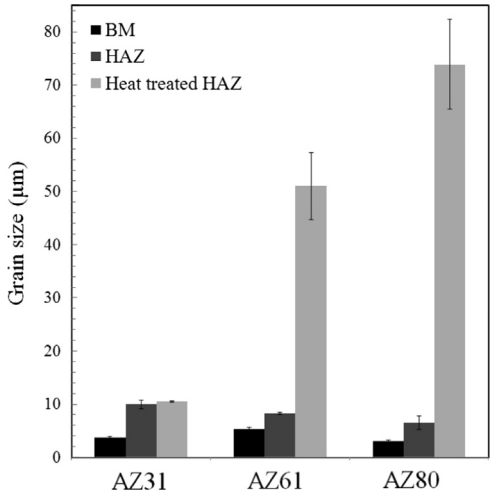

Fig. 10. Grain size in BM, HAZ and heat treated HAZ for AZ31, AZ61 and AZ80.

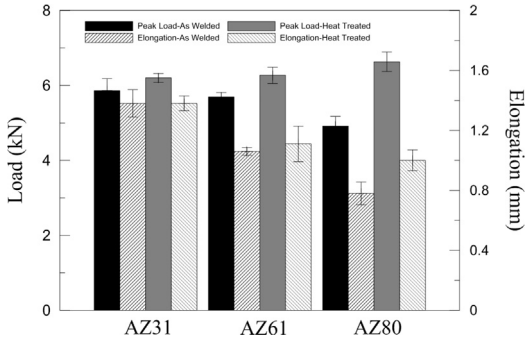

Fig. 11. Failure peak load and specimen elongation (at the peak load) values of the three welds in as-welded and heat treated conditions.

growth occurred near the saturation limit in the HAZ of AZ31 during the welding cycle and no significant further growth occurred during the PWHT.

3.4. Mechanical properties of the welds

Fig. 11 compares the tensile shear peak load and elongation of the spot welded Mg alloys in both as-welded and heat-treated conditions. Three different failure modes were observed after the tensile shear test: interfacial, nugget pull-out and through-thickness. The schematics of the aforementioned failure modes

are shown in Fig. 12. The AZ61 and AZ80 as-welded samples suffered from nugget pull-out failure in tensile shear testing, and the AZ31 weld samples failed by interfacial mode. The failure mode of the AZ61 and AZ80 weld samples changed from nugget pullout to through-thickness due to the PWHT, while PWHT had no obvious effect on the failure mode of AZ31 which was interfacial.

The force required to cause failure of a spot weld is equal to the product of material strength and failed area of cross section. It has been found that the failure load for the pull out/through-thickness fracture depends strongly on the sheet thickness and nugget diameter; however the load to cause interfacial failure is correlated more with the nugget diameter and less on sheet thickness [36,37]. The following equations were reported to predict the material strength based on the failure mode [36]:

$$\sigma_{UT} = \frac{F_{PO}}{k_{PO} dt}. \quad (1)$$

$$\sigma_{UT} = \frac{F_{IF}}{k_{IF} d^2}. \quad (2)$$

where F_{PO} and F_{IF} are failure loads for pull-out and interfacial modes respectively, σ_{UT} is the tensile strength of the material, d is the nugget diameter and t is the sheet thickness. k_{PO} ($\sim$2.2) and k_{IF} ($\sim$0.6) are constants which were determined from a combination of finite element modeling and fracture mechanics calculations [36]. Table 2 shows the calculated tensile strengths of the welds by Eq. (1) for pull-out/through thickness fractured samples (i.e. AZ61 and AZ80 welds) and by Eq. (2) for samples failed by interfacial fracture (i.e. AZ31 welds). The nugget diameter was measured optically from the weld cross section. The increases in average strength values of the welds after PWHT were determined to be +3.1%, +11.7% and +37.2% for AZ31, AZ61 and AZ80 respectively. In summary, PWHT had considerable effects on the strength and failure mode of high Al content welds; however, such effects were not pronounced in the low Al content welds (i.e. AZ31).

The change in the failure mode and strength of high Al content welds (AZ61 and AZ80) due to PWHT is associated with the change in the crack propagation path. "Peak hold" tensile shear tests were conducted in order to study the crack propagation path. Fig. 13 shows the typical cross-sectional crack path of the AZ61 welds in as welded and heat treated conditions. For all the samples cracks always started from the notch where the two base metal surfaces were joined by the RSW nugget. Then cracking propagated along the fusion boundary of as-welded test samples but mainly located in the HAZ (Fig. 13a). For the post-weld heat treated samples, the crack propagated inside the HAZ/base metal (BM) regions and far away from the fusion boundary (Fig. 13b). Significant traces of twinning were also found near the crack edges, suggesting that the micro-deformation of the α-Mg lattice occurred ahead of the crack front. Similar observations were made for the AZ80 weld samples, which were reported in our previous report [24].

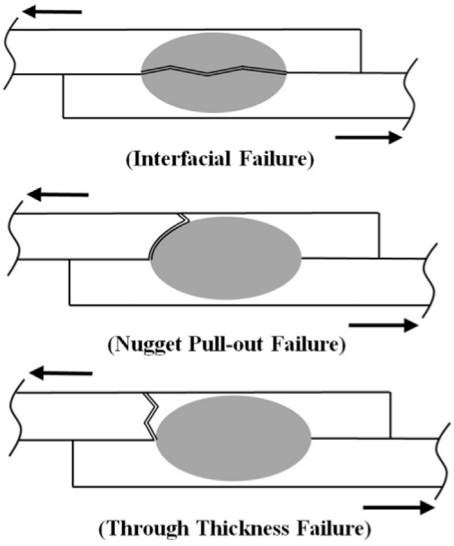

Fig. 12. Schematic of the three failure modes observed in this study.

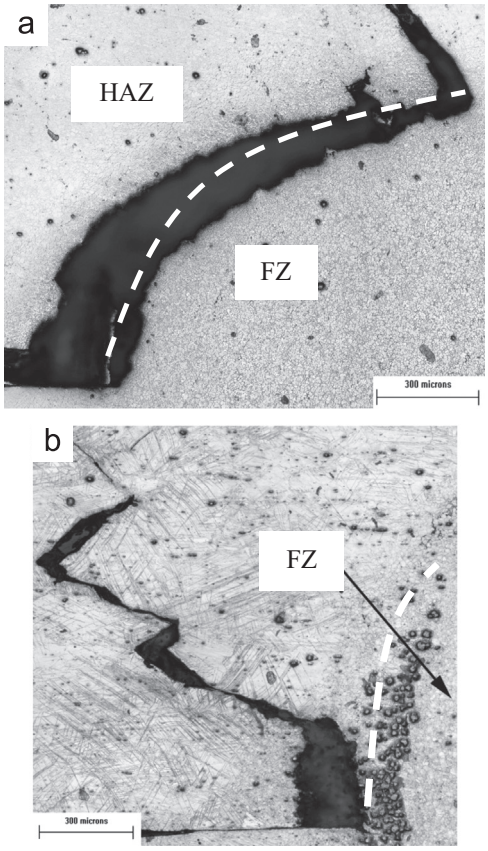

Fig. 13. Typical crack propagation path of the AZ61 RSW weld samples in (a) as-welded condition and (b) heat treated condition.

Table 2
Average tensile strength of the weld in the as welded and heat treated conditions.

	As welded		Heat treated	
	Failure mode	Tensile strength (MPa)	Failure mode	Tensile strength (MPa)
AZ31	Interfacial	109.6	Interfacial	113.0
AZ61	Pull-out	129.2	Through Thickness	139.2
AZ80	Pull-out	109.0	Through Thickness	149.5

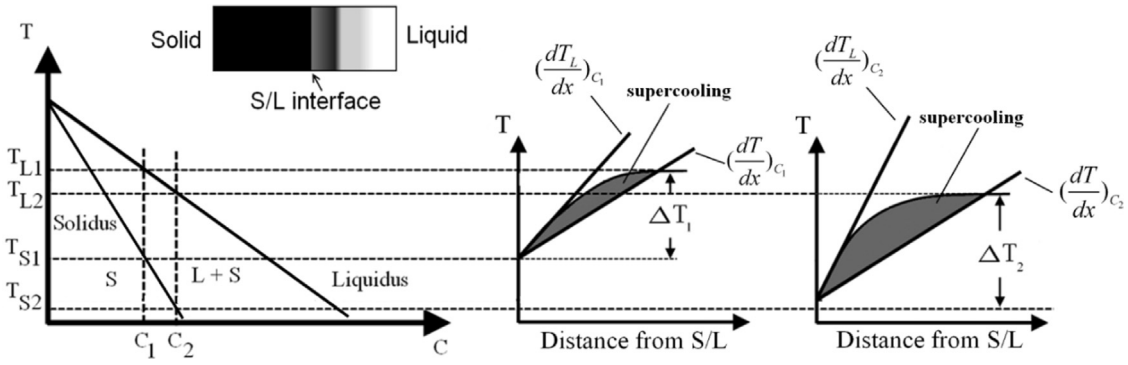

Fig. 14. Schematic of supercooling for solidification of imaginary alloys 1, 2 ($C_2 > C_1$).

4. Discussion

4.1. Columnar to equi-axed transition and grain refinement

Enhanced columnar to equi-axed transition (CET) and grain refinement, by increase in the solute content, is justified by the constitutional supercooling ahead of the solidification front. As illustrated schematically in Fig. 14, the extent of supercooling can be defined by the area limited to the actual thermal gradient present in the FZ (dT/dx) and the "critical temperature gradient" (dT_L/dx) which is proportional to the concentration of the solute in the liquid metal (C_0) [38]:

$$\frac{dT_L}{dx} = \frac{mC_0(1-k)v}{kD}. \quad (3)$$

where C_0 is the solute concentration, k is the equilibrium partition coefficient, m is the liquidus slope, υ is the solidification rate and D is the diffusivity coefficient in liquid state. According to Eq. (1) critical temperature gradient increases as the liquid metal is enriched more in solute content. Considering that the actual temperature gradient is the same in solidification of welds of the three alloys (as the same welding parameters were used for joining of the three alloys), it is proposed that more supercooling is provided for solidification of welds with more alloying content. The supercooling-driven nucleation model proposed by Winegard and Chalmers suggested that the increase in supercooling, due to solute enrichment, enhanced the heterogeneous nucleation rate (N_{het}) on the available substrate nucleants [39]. In the current study the Al–Mn particles shown in Fig. 6 (either pre-existing in the BM or formed during the early stage of solidification), could be able to act as heterogeneous nucleants. The heterogeneous nucleation was reported to take place in the RSW microstructure by the Al–Mn particles pre-existing in the BM of magnesium alloys [20,40]. As the solute content increased from AZ31 to AZ80, it is expected that $N_{het}(\text{AZ31}) < N_{het}(\text{AZ61}) < N_{het}(\text{AZ80})$.

4.2. Crystallographic orientation relationships in α-Mg/β

Generally the divorced eutectic phase grows from the remaining liquid in the inter-dendritic regions at the late stage of the solidification. The growth of eutectic phase is done in such a way that certain OR will be established with minimum energy [41]. It was proposed by Shiflet and van der Merwe that the minimum interfacial energy is obtained when the close packed or nearly close packed atomic rows match at the interface [42]. On the other hand a set of close packed or nearly close packed planes from the two phases should be arranged in such a way to achieve the edge to edge matching [43]. It has been found that the {3 3 0} (41.9% close-packed) and {4 1 1} (44.6% close-packed) are both the nearly close-packed planar types in the $Mg_{17}Al_{12}$ lattice [44,45] with the same d spacing of 2.48 Å. Fig. 15 shows the atom configuration of the β lattice in the (3 3 0) plane. The unit cell was reconstructed based on the position of the Mg and Al atoms as shown in Table 3 [5,46]. In HCP structure, the most close-packed planes are {0 0 0 2} (100% close-packed) and $\{\bar{1}\ 0\ 1\ 1\}$ (81% close-packed). Consequently, the determined planar relationships i.e. {0 0 0 2}//{3 3 0} and $\{1\ 0\ \bar{1}\ 1\}$//{3 3 0} are expected in order to minimize the interfacial energy. The d-value mismatch calculations also predicted a fairly good planar matching (δ=4.8% for {0 0 0 2}//{3 3 0} and δ=1.3% for $\{1\ 0\ \bar{1}\ 1\}$//{3 3 0}). The crystallographic OR was determined for the HR-TEM image in Fig. 7b as follows:

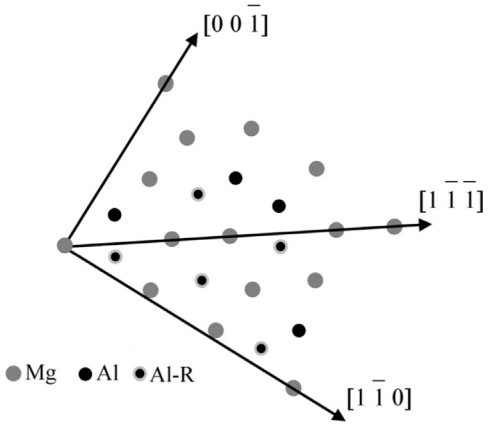

Fig. 15. Atomic arrangement on (3 3 0) plane of β unit cell. The {3 3 0} planes are not flat, but "corrugated", i.e. some of the Al atoms (as indicated by Al-R) have the centers which are not exactly located on the plane. The maximum displacement of the centers of such atoms normal to plane normal is 1.32 Å.

$$[2\ \bar{1}\ \bar{1}\ 0]_\alpha\ //\ [1\ \bar{1}\ 1]_\beta,\ (0\ 0\ 0\ 2)_\alpha//(0\ 3\ 3)_\beta \quad \text{OR.1}$$

The interatomic misfit along the matching direction for this OR was calculated to be 5.3%. Thus high atomic matching is expected to exist at the interface with low strain energy. This has been demonstrated in Fig. 16a. This OR is close to the OR defined by Potter [47]. Such relationship was previously confirmed by Zhang and Kelly [48] for precipitation hardened Mg–Al alloys. They proposed that such atomic row matching satisfied the requirements for the edge to edge matching model in order to obtain a low interfacial energy (i.e. interatomic misfit $\leq$10%).

In case of the orientation relationship corresponding to Fig. 8d, high interatomic mismatch exists between the two parallel directions along the diffraction pattern zone axis i.e. $<\bar{1}\ 5\ \bar{4}\ \bar{3}>$ (9.97 Å) of Mg and $<\bar{1}\ 1\ 1>$ of the β (3.05 Å). In addition, the $<1\ \bar{5}\ \bar{4}\ \bar{3}>$ (which are $<1\ 3\ \bar{1}>$ according to three values Miller indices) are not considered as close packed directions in Mg

Table 3
Atom position in β-$Mg_{17}Al_{12}$ unit cell (the values were taken from Ref. [5]).

Atom	Multiplicity	Site Symmetry	Coordinates: (0,0,0)+ (0.5,0.5,0.5)+		
			x	y	z
Mg	2	$\bar{4}3m$	0	0	0
Mg	8	.m	0.324	0.324	0.324
Mg	24	..m	0.3582	0.3582	0.0393
Al	24	..m	0.0954	0.0954	0.2725

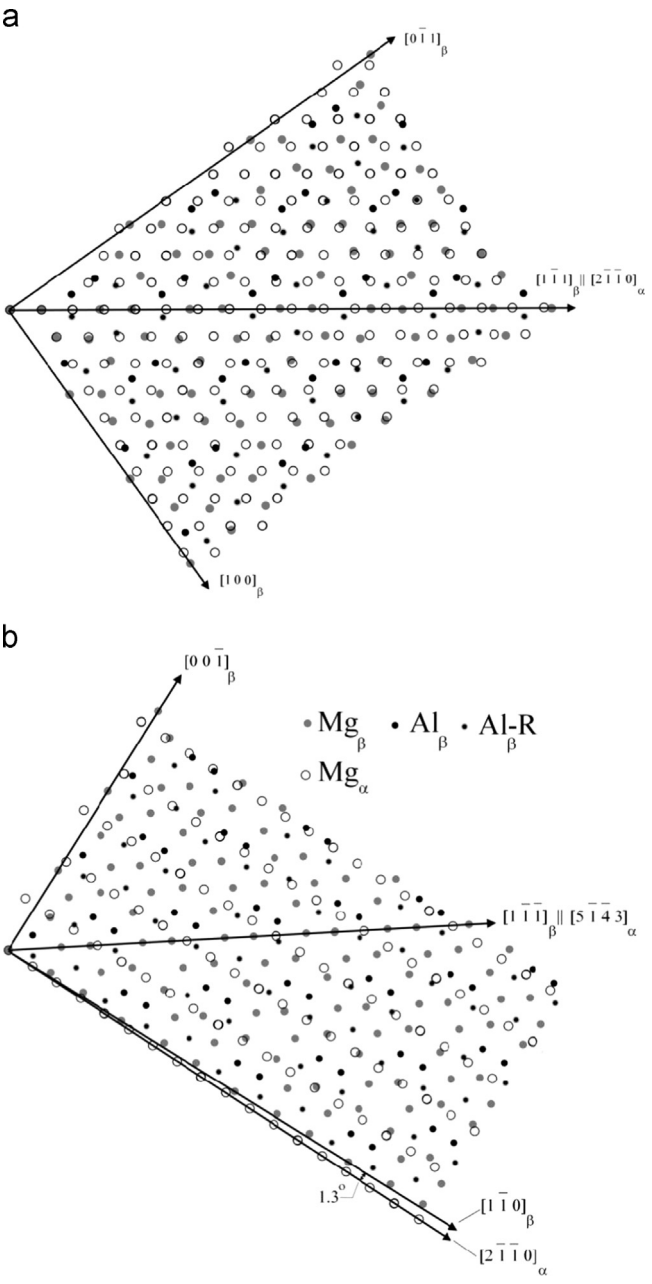

Fig. 16. Atomic arrangement of (a) $(0\,0\,0\,2)_\alpha$ and $(0\,3\,3)_\beta$; (b) $(0\,\bar{1}\,\bar{1}\,1)_\alpha$ and $(3\,3\,0)_\beta$.

lattice. Consequently another direction matching should exist between the two phases. Fig. 16b shows the atomic arrangement of $(0\,\bar{1}\,\bar{1}\,1)_\alpha$ and $(3\,3\,0)_\beta$. It is seen that excepting the parallelism of $[\bar{1}\,5\,\bar{4}\,\bar{3}]_\alpha$ and $[\bar{1}\,1\,1]_\beta$, very small misalignment (1.2°) exists between the $[2\,\bar{1}\,\bar{1}\,0]_\alpha$ and $[1\,\bar{1}\,0]_\beta$. The [1 1 0] direction is

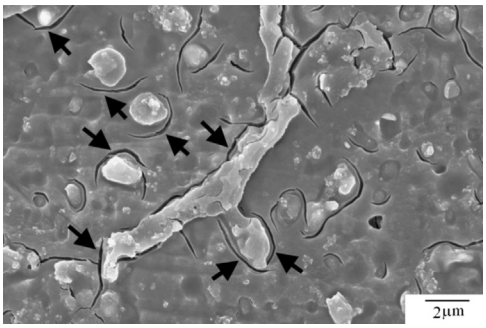

Fig. 17. Microstructure near the crack region for the AZ80 weld in the as-welded condition.

considered as a nearly close packed atomic row in the β lattice. Thus the following OR can be proposed for this particle:

$$[2\,\bar{1}\,\bar{1}\,0]_\alpha // [1\,\bar{1}\,0]_\beta,\ (0\,\bar{1}\,\bar{1}\,1)_\alpha // (3\,3\,0)_\beta \qquad \text{OR.2}$$

The interatomic misfit along the matching directions was calculated to be 54.8%. Based on the edge-to-edge matching model [43], this misfit value is significantly large. Therefore, the interfacial boundary between the β particle and Mg matrix is expected to be incoherent.

4.3. Crack propagation

In this study OR.2 was confirmed between a GB particle and grain 1 as demonstrated in Fig. 7a with fairly high atomic matching; however, no OR was found between the same particle and grain 2. It can be proposed that the eutectic growth occurred on grain 1 (or dendrite) and therefore OR was fixed. The divorced eutectic phase was not able to build an OR with the adjacent solidifying grain (grain 2) as the restrictive crystallographic matching of the particle with grain 1 was unlikely to produce a favorable OR with the grain 2 [49]. This is also true for the GB particles in the HAZ. In case of OR (2), poor atomic matching is expected to exist at the interface. It can also be inferred via Fig. 16 that as the particle/matrix interface grows larger (as the particle size increases), the atomic matching becomes more difficult and the coherency strains are replaced by the dislocations. Therefore, it is implied that the interfacial energy between the GB particles and Mg matrix is high and a high concentration of dislocations exists at the interface. Due to high interfacial energy, de-cohesion of particle/matrix is expected [10] by the application of external stress, leading to production of micro-cracks at either particle/matrix interface or in Mg matrix close to the interface, as observed in Fig. 17. The increase in crack propagation rate, by the growth and coherency loss of the particles, was reported in aged aluminum alloys [11]. On the other hand, the particles present within the Mg grains enhanced void formation due to the surrounding plastic flow which resulted in further crack propagation [10,11,24].

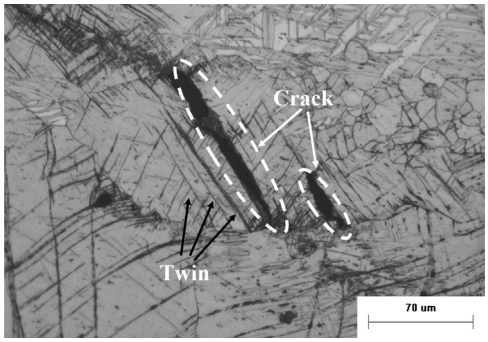

Fig. 18. Microstructure of the HAZ of AZ61 in heat treated condition (the weld was subjected to tensile shear test up to peak load).

The formation of micro-cracks and micro-voids in the HAZ enhanced the crack propagation in high Al weld samples. The primary crack preferred to propagate along the GBs as they contained the continuous network of β intermetallics. It is possible that the fracture could occur within the FZ, where high concentration of β particles exist; however fracture path in the FZ is tortuous due to dendritic morphology of the microstructure. Thus, the crack preferentially propagated along the GBs in the HAZ.

Unlike AZ61 and AZ80, insignificant formation of the β particles occurred in the HAZ of AZ31 (Fig. 5b). Thus, the HAZ microstructure was more resistant against cracking. The crack preferably initiated/propagated into the developed columnar structure of the FZ in AZ31 leading to interfacial fracture. It was previously reported that the developed columnar structure formed near the fusion boundary of AZ31 is the preferred crack growth path [23].

The β particles are dissolved into the Mg matrix via post-weld heat treatment. Thus, the potential sites for the easy crack propagation were removed. Within the heat treated microstructure of the weld, the crack appeared to grow by formation of plastic zones ahead of its front. This can be confirmed via observation of heavily twinned microstructure near the crack region (Fig. 18). A direct linkage between crack formation and the $\{1\,0\,\bar{1}\,1\}-\{1\,0\,\bar{1}\,2\}$ double twinning was previously found in AZ magnesium alloys [50–55]. Due to their favorable orientation for basal slip, these twins created a highly localized shear deformation region. It was proposed by Meyers that the twinning becomes more difficult with grain refinement in HCP-structured materials [56]. The improvement in fracture toughness of magnesium alloys has been reported with grain refinement [17,18]. From a comparison of Figs. 9a and b, grain size in the FZ appeared to be larger than that in the HAZ. Such coarse-grained microstructure is more prone to twin formation during stress application. On the contrary, grain refinement occurred in the FZ of AZ61 and AZ80 alloys. This fine grain microstructure was stable even after PWHT as shown in Fig. 9c,d; however, severe grain growth occurred during PWHT in the HAZ. Therefore, in the case of AZ61 and AZ80 alloys, twins formed more readily in the HAZ than in the FZ. Cracking would therefore be reasonably expected to initiate within such twins inside the HAZ microstructure as observed in Fig. 18.

A coarse-grained microstructure was present in the FZ of AZ31 (Fig. 5a) due to low heterogeneous nucleation rate. These grains became coarsened during the PWHT. Moreover, unfavorable elongated grains emerged from the columnar dendrites initially formed adjacent to the fusion boundary (Fig. 3a). On the other hand, HAZ grains remained small during the PWHT of AZ31 welds (Fig. 10). Thus the failures continued to be interfacial in the post-weld heat treated AZ31 welds.

5. Conclusions

This work has been concerned with the effects of Al content on the microstructure and mechanical performance of resistance spot welds in three AZ magnesium alloys. The following conclusions have been drawn:

(1) The columnar to equi-axed transition and grain refinement were enhanced as the Al content of magnesium base alloy increased. The increase in the solute content increased constitutional supercooling, which led to promotion of heterogeneous nucleation during solidification and grain refinement.
(2) The weld strength order AZ31 > AZ61 > AZ80 is opposite to that of base materials of AZ31 < AZ61 < AZ80, since easy crack initiation at the β/matrix interfaces in the HAZ of AZ61 and AZ80 welds occurred, adjacent to the fusion line.
(3) Post-weld heat treatment significantly removed the beta phase particles and resulted in improved tensile shear strength of high Al content welds (AZ61 and AZ80). This is because the cracking propagated away from the fusion boundary into base metal (heat affected zone).
(4) With the absence of the secondary phase, the failure mode demonstrated strong dependence on the grain size: fractures occurred through the heat affected zone for AZ61 and AZ80 welds due to their larger grains compared to those in the fusion zone. On the other hand, cracks preferentially propagated in the fusion zone of AZ31, where larger grains were formed in the fusion zone compared to those in the heat affected zone.

Acknowledgments

This research is financially supported by the NSERC Magnesium Network (MagNET) and Magnesium Front End Research and Development (MFERD). The authors would like to thank Research Institute of Industrial Science and Technology (RIST) and POSCO for providing the magnesium sheets.

References

[1] S. Zhang, Int. J. Fract. 88 (1997) 67–85.
[2] S. Zhang, Weld. J. 78 (1999) 173–179.
[3] S. Zhang, Int. J. Fract. 112 (2001) 247–274.
[4] L.P. Pook, Int. J. Fract. 11 (1975) 173–176.
[5] P. Villars, L.D. Calvert, Pearson's Handbook of Crystallographic Data for Intermetallic Phases, first ed., ASM, Metals Park, 1985.
[6] C.T. Chi, C.G. Chao, T.F. Liu, C.H. Lee, Scr. Mater. 56 (2007) 733–736.
[7] C.T. Chi, C.G. Chao, J. Mater. Process. Technol. 182 (2007) 369–373.
[8] Y. Quan, Z. Chen, X. Gong, Z. Yu, Mater. Sci. Eng. A 496 (2008) 45–51.
[9] S.F. Su, J.C. Huang, H.K. Lin, N.J. Ho, Metall. Mater. Trans. A 33 (2001) 1461–1473.
[10] M.N. Desmukh, R.K. Pandey, A.K. Mukhopadhyay, Mater. Sci. Eng. A 435 (2006) 318–326.
[11] J.Z. Chen, L. Zhen, S.J. Yang, S.L. Dai, Trans. Nonferr. Met. Soc. 20 (2010) 2209–2214.
[12] Z. Wang, M. Gao, H. Tang, Mater. Charact. 62 (2011) 943–951.
[13] O. Sabokpa, A. Zarei-Hanzaki, H.R. Abedi, Mater. Sci. Eng. A 550 (2012) 31–38.
[14] H.A. Patel, D.L. Chen, S.D. Bhole, K. Sadayappan, J. Alloys Compd. 496 (2010) 140–148.
[15] B. Kim, J. Do, S. Lee, I. Park, Mater. Sci. Eng. A 527 (2010) 6745–6757.
[16] Y. Wang, G. Liu, Z. Fan, Scr. Mater. 54 (2006) 903–908.
[17] H. Somekawa, T. Mukai, Scr. Mater. 53 (2005) 1059–1064.
[18] H. Somekawa, T. Mukai, Scr. Mater. 53 (2005) 541–545.
[19] H. Somekawa, T. Mukai, Scr. Mater. 54 (2006) 633–638.
[20] L. Xiao, L. Liu, Y. Zhou, S. Esmaeili, Metall. Mater. Trans. A 41 (2010) 1511–1522.
[21] L. Xiao, L. Liu, S. Esmaeili, Y. Zhou, Metall. Mater. Trans. A 43 (2011) 598–609.
[22] L. Xiao, L. Liu, D.L. Chen, S. Esmaeili, Y. Zhou, Mater. Sci. Eng. A 529 (2011) 81–87.
[23] L. Liu, L. Xiao, J.C. Feng, Y.H. Tian, S.Q. Zhou, Y. Zhou, Metall.. Mater. Trans. 41 (2010) 2651–2661.

[24] S.T. Niknejad, L. Liu, T. Nguyen, M.Y. Lee, S. Esmaeili, Y. Zhou, Metall.. Mater. Trans. A 44 (2013) 3747–3756.
[25] T. Zhu, Z.W. Chen, W. Gao, J. Alloys Compd. 501 (2010) 291–296.
[26] S. Barbagallo, H.I. Laukli, O. Lohne, E. Cerri, J. Alloys Compd. 378 (2004) 226–232.
[27] M.H.F. Overwijk, F.C. van den Heuvel, J. Vac. Sci. Technol. B 11 (1993) 2021–2024.
[28] C. Huang, S. Kou, Weld. J. 5 (2000) 113–120.
[29] C.W. Bale, E. Bélisle, P. Chartrand, S.A. Decterov, G. Eriksson, K. Hack, I.H. Jung, Y.B. Kang, J. Melançon, A.D. Pelton, C. Robelin, S. Petersen, CALPHAD 33 (2009) 295–311.
[30] M. Ohno, R. Schmid-Fetzer, Z. Metallkd. 96 (2005) 857–869.
[31] J.C. Feng, Y.R. Wang, Z.D. Zhang, Sci. Technol. Weld. 11 (2006) 154–162.
[32] J.J. Pepe, W.F. Savage, Weld. J. 46 (1967) 411–422.
[33] J.J. Pepe, W.F. Savage, Weld. J. 49 (1970) 545–553.
[34] I.A. Aksay, C.E. Hoge, J.A. Pask, J. Phys. Chem. 78 (1974) 1178–1183.
[35] B. Radhakrishnan, R.G. Thompson, Met. Trans. A 24 (1993) 2773–2785.
[36] D.J. Radakovic, M. Tumuluru, Weld. J. 87-S (2008) 96–105.
[37] Y.J. Chao, Sci. Technol. Weld. 8 (2003) 133–137.
[38] W. Kurz, D.J. Fisher, Fundamentals of Solidification, fourth ed., Trans Tech Publication, Switzerland, 1986.
[39] W.C. Winegard, B. Chalmers, Trans. Am. Soc. Met. 46 (1954) 1214–1227.
[40] L. Liu, L. Xiao, J. Feng, L. Li, S. Esmaeili, Y. Zhou, Scr. Mater. 65 (2011) 982–985.
[41] S. Guldberg, N. Ryum, Mater. Sci. Eng. A 289 (2000) 143–150.
[42] G.J. Shiflet, J.H. van der Merwe, Metall. Mater. Trans. A 25 (1994) 1895–1903.
[43] P.M. Kelly, P.M. Zhang, Metall. Mater. Trans. A 37 (2006) 833–839.
[44] J.F. Nie, X.L. Xiao, C.P. Luo, B.C. Muddle, Micron 32 (2001) 857–863.
[45] P. Kelly, H.P. Ren, D. Qiu, M.X. Zhang, Acta Mater. 58 (2010) 3091–3095.
[46] T. Hahn, International Tables for Crystallography Volume A, D. Reidel Publishing Company, Dordrecht, Boston, 1983.
[47] D.I. Potter, J. Less-Common Met. 31 (1973) 299–309.
[48] M.X. Zhang, P.M. Kelly, Scr. Mater. 48 (2003) 647–652.
[49] D.A. Porter, K.E. Easterling, Phase Transformation of Metals and Alloys, second ed., Chapman & Hall, London, 1992.
[50] H. Somekawa, T. Inoue, T. Mukai, Mater. Sci. Eng. A 527 (2010) 1761 (1761).
[51] M.H. Yoo, Metall. Mater. Trans. 12 (1981) 409–418.
[52] J. Koike, N. Fujiyama, D. Ando, Y. Sutou, Scr. Mater. 63 (2010) 747–750.
[53] R.E. Reed-Hill, W.D. Robertson, Acta Metall. 5 (1957) 717–726.
[54] P. Cizek, M.R. Barnett, Scr. Mater. 59 (2008) 959–962.
[55] D. Ando, J. Koike, Y. Sutou, Acta Mater. 58 (2010) 4316–4324.
[56] M.A. Meyers, O. Vohringer, V.A. Lubarda, Acta Mater. 49 (2001) 4025–4039.